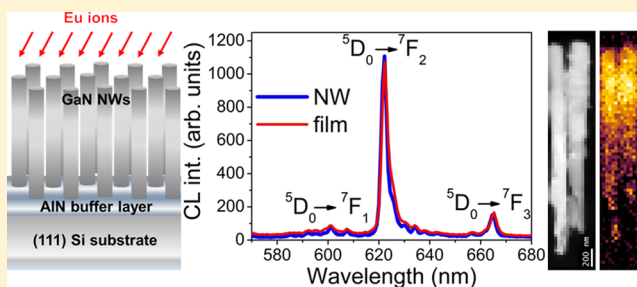


## Incorporation of Europium into GaN Nanowires by Ion Implantation

D. Nd. Faye,<sup>†</sup> X. Biquard,<sup>‡</sup> E. Nogales,<sup>§</sup> M. Felizardo,<sup>†</sup> M. Peres,<sup>†</sup> A. Redondo-Cubero,<sup>†,○</sup>  
T. Auzelle,<sup>||,⊥</sup> B. Daudin,<sup>||</sup> L. H. G. Tizei,<sup>⊥,Ⓛ</sup> M. Kociak,<sup>⊥,Ⓛ</sup> P. Ruterana,<sup>#</sup> W. Möller,<sup>¶</sup> B. Méndez,<sup>§,Ⓛ</sup>  
E. Alves,<sup>†</sup> and K. Lorenz<sup>\*,†,∇,Ⓛ</sup><sup>†</sup>IPFN, Instituto Superior Técnico, Universidade de Lisboa, Campus Tecnológico e Nuclear, Estrada Nacional 10, 2695-066 Bobadela LRS, Portugal<sup>‡</sup>Université Grenoble Alpes, CEA, IRIG, MEM, NRS, 38000 Grenoble, France<sup>§</sup>Departamento de Física de Materiales, Universidad Complutense, 28040 Madrid, Spain<sup>||</sup>Université Grenoble Alpes, CEA, IRIG, PHELIQS, 38000 Grenoble, France<sup>⊥</sup>Laboratoire de Physique des Solides, Université Paris-Sud, CNRS-UMR 8502, Orsay 91405, France<sup>#</sup>Centre de recherche sur les Ions les Matériaux et la Photonique (CIMAP), UMR 6252, CNRS-ENSICAEN, Boulevard Maréchal Juin, 14050 Caen, France<sup>¶</sup>Institute of Ion Beam Physics and Materials Research, Helmholtz-Zentrum Dresden-Rossendorf, Bautzner Landstraße 400, D-01328 Dresden, Germany<sup>∇</sup>Instituto de Engenharia de Sistemas de Computadores-Microsistemas e Nanotecnologias (INESC-MN), Rua Alves Redol 9, 1000-029 Lisboa, Portugal

## Supporting Information

**ABSTRACT:** Rare earth (RE)-doped GaN nanowires (NWs), combining the well-defined and controllable optical emission lines of trivalent RE ions with the high crystalline quality, versatility, and small dimension of the NW host, are promising building blocks for future nanoscale devices in optoelectronics and quantum technologies. Europium doping of GaN NWs was performed by ion implantation, and structural and optical properties were assessed in comparison to thin film reference samples. Despite some surface degradation for high implantation fluences, the NW core remains of high crystalline quality with lower concentrations of extended defects than observed in ion-implanted thin films. Strain introduced by implantation defects is efficiently relaxed in NWs and the measured deformation stays much below that in thin films implanted in the same conditions. Optical activation is achieved for all samples after annealing, and while optical centers are similar in all samples, Eu<sup>3+</sup> emission from NW samples is shown to be less affected by residual implantation damage than for the case of thin films. The incorporation of Eu in GaN NWs was further investigated by nano-cathodoluminescence and X-ray absorption spectroscopy (XAS). Maps of the Eu-emission intensity within a single NW agree well with the Eu-distribution predicted by Monte Carlo simulations, suggesting that no pronounced Eu-diffusion takes place. XAS shows that 70–80% of Eu is found in the 3+ charge state while 20–30% is 2+ attributed to residual implantation defects. A similar local environment was found for Eu in NWs and thin films: for low fluences, Eu is mainly incorporated on substitutional Ga-sites, while for high fluences XAS points at the formation of a local EuN-like next neighbor structure. The results reveal the high potential of ion implantation as a processing tool at the nanoscale.



## 1. INTRODUCTION

Rare earth-doped GaN thin films have been the subject of intense research in the past 2 decades due to their promising properties for optoelectronic and spintronic applications.<sup>1</sup> In particular, doping with europium led to the demonstration of the first low voltage GaN:Eu light-emitting diode (LED).<sup>2</sup> The typical red luminescence of the Eu<sup>3+</sup> ions is of particular interest since the efficiency of conventional III-nitride LEDs drops significantly in the green and red spectral region.<sup>3</sup> While GaN:Eu films have been fabricated by various techniques such

as in situ doping during molecular beam epitaxy (MBE)<sup>4</sup> and metal organic vapor phase epitaxy<sup>2</sup> or ex situ doping by ion implantation,<sup>5,6</sup> studies on Eu-doped GaN nanowires (NWs) are still scarce.<sup>7–9</sup> Given the demonstrated advantages of GaN NWs (e.g., grown by MBE) over epitaxial films, including low dislocation densities, their ability of efficient strain relaxation

Received: December 13, 2018

Revised: March 17, 2019

Published: April 2, 2019

even on lattice mismatched substrates, and improved light extraction,<sup>10</sup> functionalization of these NWs with optically active ions could lead the way to new applications and device designs. However, in situ doping of NWs is challenging due to frequently occurring segregation of second phases or morphology changes. Furthermore, so-called self-purification processes cause the expulsion of dopants from the bulk of the NWs to their surface. Aravindh and Roqan, based on density functional theory calculations, suggest that the most likely incorporation sites of the rare earth Gd in GaN NWs are at the surface.<sup>11</sup> Xu et al.<sup>7</sup> fabricated Eu-doped GaN nanoneedles via a vapor transport route with the dominant  $\text{Eu}^{3+}$  emission line, corresponding to the  ${}^5\text{D}_0 \rightarrow {}^7\text{F}_2$  intra-atomic transition, at 611 nm. Typical wavelengths for the main line of various optically active  $\text{Eu}^{3+}$  centers in GaN:Eu films lie in the range from 618 to 625 nm.<sup>12</sup> The large shift of the emission to higher energy for the case of the nanoneedles can be attributed to surface effects.<sup>7</sup> Confinement effects should play a negligible role in this behavior since only minor shifts due to site multiplicities or different strain states were reported for rare earths incorporated in quantum dots and NWs.<sup>13,14</sup> Sekiguchi et al.,<sup>9</sup> reported the Eu-doping of GaN NWs during MBE growth leading to similar optical centers as in thin films while exhibiting strongly reduced concentration quenching. Despite these highly promising results, doping led to morphology changes and even polycrystalline growth for high Eu concentrations.<sup>9</sup> Ion implantation was suggested as a promising alternative to introduce dopants in NWs without affecting their morphology.<sup>15,16</sup> Indeed, establishing the ion implantation technique as processing tool at the nanoscale could facilitate the use of doped NWs as building blocks for future nanodevices in electronics and photonics. Rodrigues et al.<sup>8</sup> studied Eu implantation in GaN NWs using fluences of  $5 \times 10^{13}$  and  $3 \times 10^{15}$  at./cm<sup>2</sup> and incidence angles with respect to the *c*-axes of the vertically aligned NWs of 20 and 30°. It was shown that annealing leads to effective optical activation of the  $\text{Eu}^{3+}$  emission with higher intensity and reduced temperature quenching compared to GaN films prepared in the same conditions. Furthermore, the dominant optical center is the same in NWs and films and no significant changes were seen in the spectral shape for different fluences and implantation geometries.<sup>8</sup>

Nevertheless, ion implantation is inherently connected with defects created by the bombardment with heavy and energetic ions which can deteriorate structural and optical properties. Implantation damage build-up processes in GaN thin films are relatively well understood. In particular, they are dominated by strong dynamic annealing, which leads to the efficient recombination of point defects already during the implantation but also promotes the formation of thermally stable extended defects such as point defect clusters and stacking faults.<sup>17–20</sup> Only few studies address implantation damage mechanisms in GaN NWs.<sup>21–24</sup> Molecular dynamics simulations for Er implanted GaN NWs reveal high sputtering yields and an accumulation of defects close to the surface.<sup>24</sup> High sputtering yields and surface defects are furthermore consistent with the experimental observation of blisters at the surface of GaN NWs after implantation.<sup>22</sup> Both simulations<sup>24</sup> and experiments<sup>23</sup> reveal the introduction of hydrostatic strain by the implantation defects. In contrast, other experimental studies suggest increased dynamic annealing in GaN NWs as compared to bulk material<sup>21</sup> and for the special case of Pr-implanted GaN NWs, Pr-related luminescence was even

enhanced by the interaction with certain defects created by the implantation and annealing processes.<sup>23</sup> Thermal annealing of implantation damage is challenging in GaN due to the thermal dissociation of the crystal starting at approximately 800 °C.<sup>25</sup> This issue is aggravated for the case of NWs due to the increased surface area to volume ratio. The application of special capping layers or annealing under high nitrogen pressure, successful in GaN layers,<sup>26,27</sup> are not practical for NWs. Nevertheless, it was shown that rapid thermal annealing at 1000 °C can effectively reduce implantation damage and optically activate rare earth ions.<sup>8,23</sup>

In this work, we report a comprehensive study of the structural alterations, in particular strain and morphology changes, induced by implantation of GaN NWs. Furthermore, we advance a microscopic model for the incorporation of implanted Eu in GaN NWs and thin films.

## 2. METHODS

Vertically aligned GaN NWs have been grown by MBE on (111) Si substrates using a thin (2–3 nm) AlN buffer layer. The NW growth was performed for ~13 h at 800 °C in nitrogen rich conditions; details were published previously.<sup>28</sup> Active N flux was provided by a radio frequency  $\text{N}_2$  plasma cell and Ga flux by a standard effusion cell. N-rich conditions were used, that is a Ga/active N flux ratio of about 1/3. Deoxidation of the (111) Si substrate was performed by dipping in a 15%-HF: deionized water bath, followed by a smooth annealing in vacuum at 300 °C and next at 900 °C till reflection high energy electron diffraction observation of a clear  $7 \times 7$  reconstruction, indicative of a clean surface.<sup>28</sup>

Figure 1a–d shows scanning electron microscopy (SEM) images of the as-grown GaN NWs for sample set 1 revealing an average diameter of ~50 nm close to the center of the wafer (Figure 1a,b) and ~100 nm toward the periphery (Figure

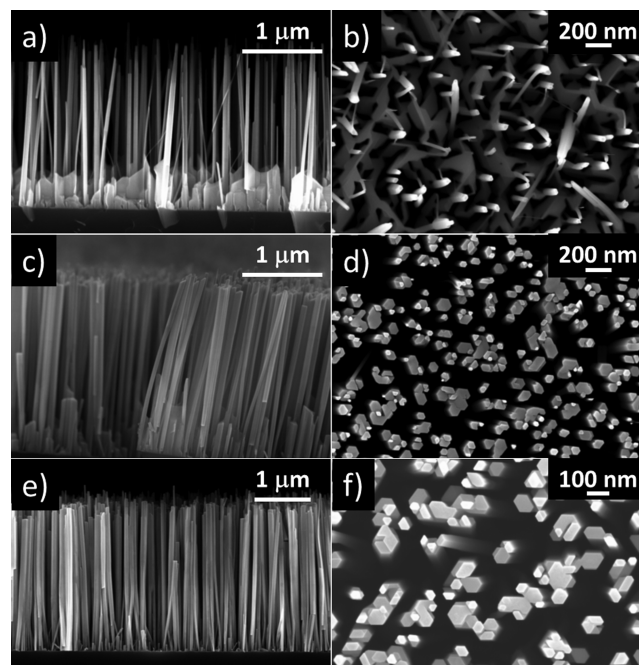


**Figure 1.** SEM side-view and top view images of the NWs used for XRD, TEM, and CL analysis (set 1) corresponding to the (a,b) wafer center and (c,d) wafer periphery. (e,f) Typical SEM images of the NWs used for XANES and EXAFS analysis (set 2).

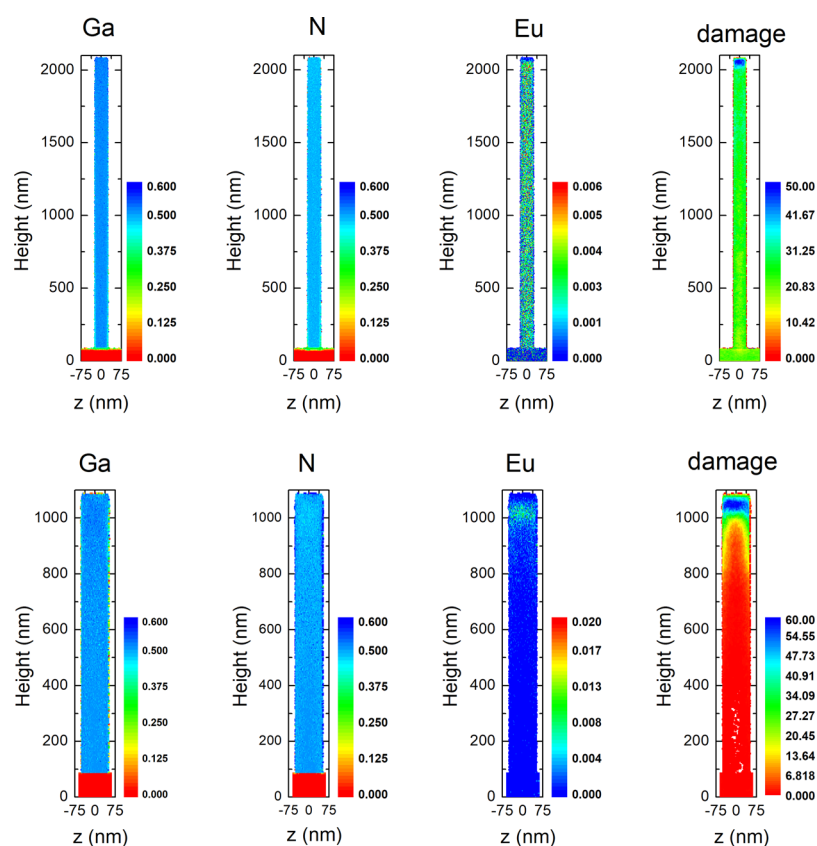


**Figure 2.** TRI3DYN simulation results showing the elemental distribution of Ga, N, and Eu (the color scale represents average atomic fraction) as well as the damage distribution (in dpa) in a longitudinal slice of 8 nm thickness along the NW length. Top: For an array of 50 nm diameter NWs with an areal density of  $2 \times 10^9 \text{ cm}^{-2}$ ; bottom: for an array of 100 nm diameter NWs and an areal density of  $7 \times 10^9 \text{ cm}^{-2}$ .

1c,d) leading to increasing coalescence when approaching the edge of the wafer. The NW length varied between 2000 and 2500 nm and the NW density ranged from 2 to  $7 \times 10^9 \text{ cm}^{-2}$  increasing toward the wafer edge. In the zones of low NW density close to the center, a 2D layer, consisting of coalesced GaN pyramids,<sup>28</sup> is visible at the base of the NWs (Figure 1a).

A second set of samples, specially designed for the synchrotron measurements, showed a more homogeneous NW density of  $9 \times 10^9 \text{ cm}^{-2}$  across the wafer and no 2D layer (Figure 1e,f).

Samples were implanted at room temperature with 300 keV Eu ions to fluences ranging from  $1 \times 10^{13}$  to  $5 \times 10^{15}$  at./cm<sup>2</sup>. Some preliminary results for implantation at 600 °C are also discussed. The implantation was done in six steps rotating the sample 60 by 60 degrees in the azimuthal angle, while the incidence angle between the beam and the NW axes was 20° for sample set 1 and 40° for sample set 2. This procedure yields a distribution of Eu and implantation defects, which is close to rotationally symmetric around the central axis of the NWs and prevents the NWs from bending due to strain gradients. The final Eu distribution inside the NWs is complex and depends on the implantation angle, NW diameter, and NW density. The three-dimensional distribution of Eu and defects has been studied using Monte Carlo simulations implemented in the TRI3DYN code.<sup>29–31</sup> This code is based on the binary collision approximation and allows simulating dynamic effects of ion irradiation in three-dimensional structures.

Annealing of the samples was performed for holding times of 30 s at 1000 °C with a heating ramp of 30 °C per second in an

ANNEALSYS halogen lamp rapid thermal processor under flowing nitrogen.

In all cases, thick ( $\sim 3 \mu\text{m}$ ) GaN layers (purchased from Lumilog) grown by metal organic chemical vapor deposition on (0001) sapphire were implanted and annealed simultaneously for comparison. Additionally, a reference layer for X-ray absorption spectroscopy (XAS) measurements was implanted along the *c*-axis to a low fluence of  $1 \times 10^{14}$  at./cm<sup>2</sup> and annealed in optimized high-temperature high-pressure (HTHP) conditions of 1400 °C and nitrogen pressure of 1 GPa.<sup>32</sup>

X-ray diffraction (XRD) was performed on a high-resolution Bruker D8 DISCOVER diffractometer using a Göbel mirror to yield a parallel beam and an asymmetric 2-bounce Ge(220) monochromator to choose the Cu  $K\alpha_1$  line.  $2\theta$ – $\theta$  curves were acquired with a 0.2 mm slit placed before the monochromator and a 0.1 mm slit in front of the scintillation detector.

Conventional transmission electron microscopy (TEM) and high-resolution scanning-TEM (STEM) were carried out on selected samples. The NWs were dispersed on the TEM grid without any further sample preparation. Conventional TEM investigations were performed with a JEOL 2100 microscope and atomically resolved STEM high-angle annular dark field images (HAADF) have been acquired in a Nion UltraSTEM 200 both operated at 200 keV.

Cathodoluminescence (CL) spectroscopy was carried out at room temperature using a Hitachi S2500 SEM and a Hamamatsu PMA-11 charge coupling device camera. The acceleration voltage was  $V_{\text{acc}} = 5 \text{ kV}$  yielding an electron penetration depth in GaN of  $\sim 70 \text{ nm}$  as estimated by the

Monte Carlo code CASINO.<sup>33</sup> The beam was defocused to several hundreds of micrometers diameter in order to limit the excitation density and mitigate the strong intensity quenching of the  $\text{Eu}^{3+}$  lines observed for a focused beam. The electron beam hits both the top surface and parts of the side facets of the NWs with an incidence angle of  $25^\circ$  toward the surface normal. Selected NW samples were furthermore analyzed using nano-CL on single NWs in a STEM (VG HB501) operated with 80 keV electrons (typical electron current 60 pA) with the sample kept at 150 K.<sup>34</sup>

XAS measurements were conducted on both FAME (BM30B) and SPLINE (BM25) beamlines at the European Synchrotron Radiation Facility (ESRF) in Grenoble, France. The main optical element of both beamlines is a two-crystal monochromator (Si(220) for FAME and Si(111) for SPLINE) with a cooled first crystal and a sagittally bent second crystal.<sup>35–37</sup> Two bendable Rh-coated mirrors located before and after the monochromator ensure harmonics rejection. XAS spectra were recorded at the  $L_{\text{III}}$  edge of Eu (6977 eV) in fluorescence mode with a multi-element energy-resolved Ge detector. Experiments were conducted at room temperature, except for the very low fluence GaN film reference sample, which was measured at 100 K to benefit from an increased signal-to-noise ratio that compensates for the very low amount of implanted Eu. The energy calibration was made using a Fe reference foil (7112 eV). Measurements were performed in grazing incidence geometry (with an angle of  $\sim 5\text{--}15^\circ$  between the beam and the sample surface) in order to maximize the signal from the implanted layer. Base line extraction of XAS spectra as well as extended X-ray absorption fine structure (EXAFS) analysis was conducted using the well-known DEMETER comprehensive system for processing and analyzing XAS data (that includes ATHENA, ARTEMIS, and IFEFFIT programs).<sup>38</sup> For meaningful quantification, we took into account the polarization of the X-ray beam. Further details on XAS measurements and data analysis are given in the Supporting Information.

### 3. RESULTS AND DISCUSSION

**3.1. Dynamic Monte Carlo Simulations.** TRI3DYN simulations have been performed for three relevant configurations: implantation of Eu at  $20^\circ$  tilt into NW arrays with either (i) 50 nm diameter and an areal density of  $2 \times 10^9 \text{ cm}^{-2}$  or (ii) 100 nm diameter and an areal density of  $7 \times 10^9 \text{ cm}^{-2}$  (corresponding to sample set 1 with samples from the center or the edge of the wafer, respectively) and (iii) implantation at  $40^\circ$  tilt into NW arrays with 100 nm diameter and an areal density of  $9 \times 10^9 \text{ cm}^{-2}$  (corresponding to sample set 2 used for XAS measurements). A regular two-dimensional square configuration of the NWs with the desired areal density is modeled by the choice of periodic lateral boundary conditions. For rotational symmetry around the axis of the NWs, the structure is randomly rotated at each ion incidence. An extended description of the simulation, including the choice of critical parameters, is included in the Supporting Information. Besides the ion energy and NW diameter, the implantation geometry and NW density will determine the distribution of Eu in the NWs due to shadowing effects by neighboring NWs. All results are shown for a final fluence of  $3 \times 10^{15} \text{ at./cm}^2$ . Figure 2 shows the simulated elemental distributions (Ga, N, Eu) in a longitudinal slice of 8 nm thickness along the NW length for cases (i) and (ii). Note that for case (ii) in the simulation a NW length of 1000 nm was assumed allowing a

better lateral resolution and saving computational costs. Figure 2 also gives the distribution of implantation damage given in displacements per atoms (dpa). For case (i) (low density of 50 nm diameter NWs), implantation yields an almost homogeneous distribution of Eu along the entire length of the wire. A slightly higher Eu concentration is found at a depth of  $\sim 55 \text{ nm}$  corresponding to ions that enter the NW from the top surface. This is seen better in Figure 3 showing the average Eu-

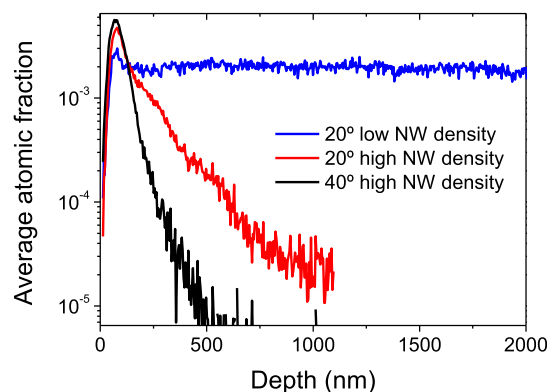


**Figure 3.** TRI3DYN simulation results showing the average atomic Eu fraction along the NW length for the three combinations of implantation angle, NW diameter, and density.

concentration along the NW length for the three cases. Accordingly, the implantation damage for case (i) is also distributed homogeneously along the entire NW with some increased displacements close to the upper surface due to ions entering the NW from the top. According to the simulations, for this low density of NWs, only about 54% of all ions are stopped within the NWs while the remaining 46% are implanted into the Si-substrate. Indeed, Rutherford back-scattering spectrometry spectra on the template after removing the NWs by scratching and ultrasound cleaning showed that a large fraction of Eu was implanted into the substrate and 2D layer in samples with low NW density. For case (ii) (high density of 100 nm diameter NWs—see bottom row of Figure 2), the distribution of Eu and implantation damage is less homogeneous. A large fraction of ions enters the NWs through the top surface leading to an increased Eu concentration in the first  $\sim 100 \text{ nm}$  of the NW (Figure 3) as well as to increased lattice damage close to the NW tip similar to implantation in planar substrates. For these implantation conditions, simulations show that 98.6% of all ions are stopped within the first 1000 nm of the NW (see Figure 3). Most ions entering through the lateral surface will not reach the NW center due to the higher NW diameter for case (ii) and Eu as well as defects will accumulate close to the rim of the NWs. The lateral distribution of Eu is shown in Figure 4, where the top row shows an integration over the first 50–150 nm of the NW tip where the Eu distribution is influenced by ions entering via the top surface leading to an almost homogeneous distribution of Eu. For integration over the remaining NW base (bottom row of Figure 4), the Eu distribution is determined by ions entering the NW from the side facets. For the 50 nm diameter NWs, this leads to a maximum Eu concentration close to the central axis of the NW while for the 100 nm diameter NWs the doping concentration is higher close to the lateral side walls and decreases toward the central axis.

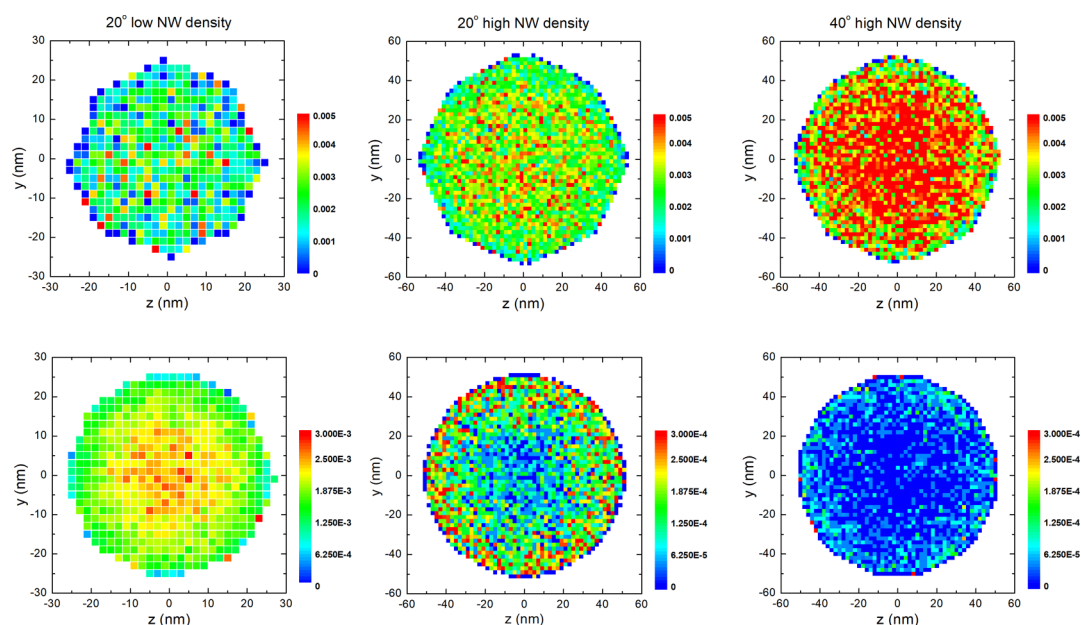


**Figure 4.** TRI3DYN simulation results showing the lateral distribution of Eu (the color scale represents average atomic fraction) for the three combinations of implantation angle, NW diameter, and density. Top: The data were integrated close to the tip of the NW corresponding to the end of range of ions entering the NW from the top. Bottom: The data were integrated from  $\sim 50$ – $150$  nm depth until the NW base in order to disregard ions that entered the NWs from the top surface.

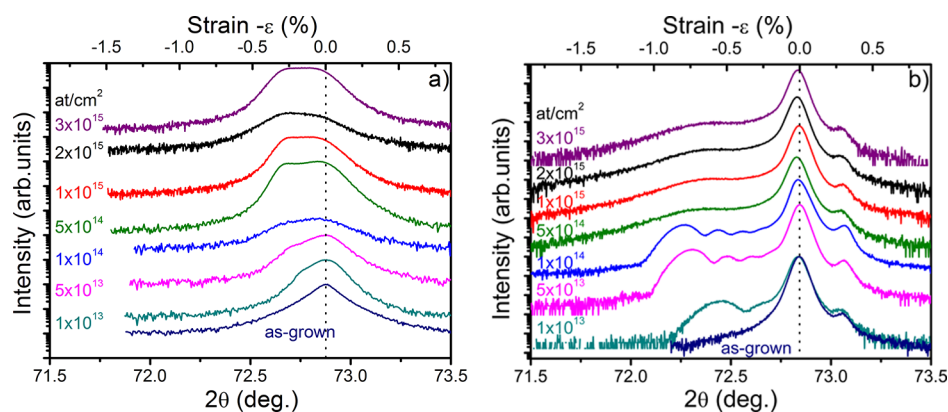


**Figure 5.** XRD (0004)  $2\theta$ - $\theta$  curves for the first set of (a) NWs and (b) reference thin films implanted to different fluences at  $20^\circ$  incidence. Note that the small peak at  $\sim 73.1^\circ$  visible in (b) is an artifact of the XRD system due to the incomplete suppression of the Cu  $K\alpha 2$  line.

For optical measurements and XRD, Eu reaching the silicon substrate does not interfere with the signal from the NWs (note that Eu is optically inactive in Si). However, for XAS measurements it is important to avoid any Eu reaching the substrate since all Eu ions will contribute to the measured signal. Therefore, the second set of samples was implanted using an incident angle of  $40^\circ$ . This geometry, together with the high and homogeneous density of NWs and the absence of a 2D layer, assured that Eu was only implanted into the GaN NWs and not into the Si-substrate or the coalesced GaN 2D layer at the base of the NWs. Figure 3 clearly shows that the Eu distribution is concentrated in the top 500 nm of the NWs. In fact, the simulations indicate that 99.3% of all ions come to rest inside the NWs while the remaining 0.7% are being backscattered.

An additional feature observed in the elemental maps in Figure 2 is a preferential loss of nitrogen due to sputtering, leading to a slight N-deficiency in the bulk of the NW, in particular, in the regions of higher damage concentration. This

is in agreement with molecular dynamics simulations of ion implantation in GaN NWs.<sup>39</sup> A slight enrichment in N is observed at the outer surface, which is attributed to the redeposition of preferentially sputtered N atoms from the surrounding NWs.

**3.2. Strain and Morphology.** Figure 5 shows XRD (0004)  $2\theta$ - $\theta$  curves for the first set of NWs and films implanted to different fluences of 300 keV Eu ions at  $20^\circ$  incidence. For the thin film reference samples, the implantation leads to the formation of a satellite peak at lower  $2\theta$  angle than the main Bragg peak clearly visible for the lowest fluence. The hydrostatic strain caused by implantation defects leads to an expansion of the  $c$ -lattice parameter within the implanted volume as it was first reported by Liu et al. for  $c$ -plane GaN layers.<sup>40</sup> With increasing fluence, the induced strain increases and the satellite peak shifts to lower angles. For fluences starting from  $5 \times 10^{14}$  at./cm<sup>2</sup>, the diffraction intensity of the satellite peak decreases strongly and XRD becomes insensitive to further defect formation. Similar curves have been reported

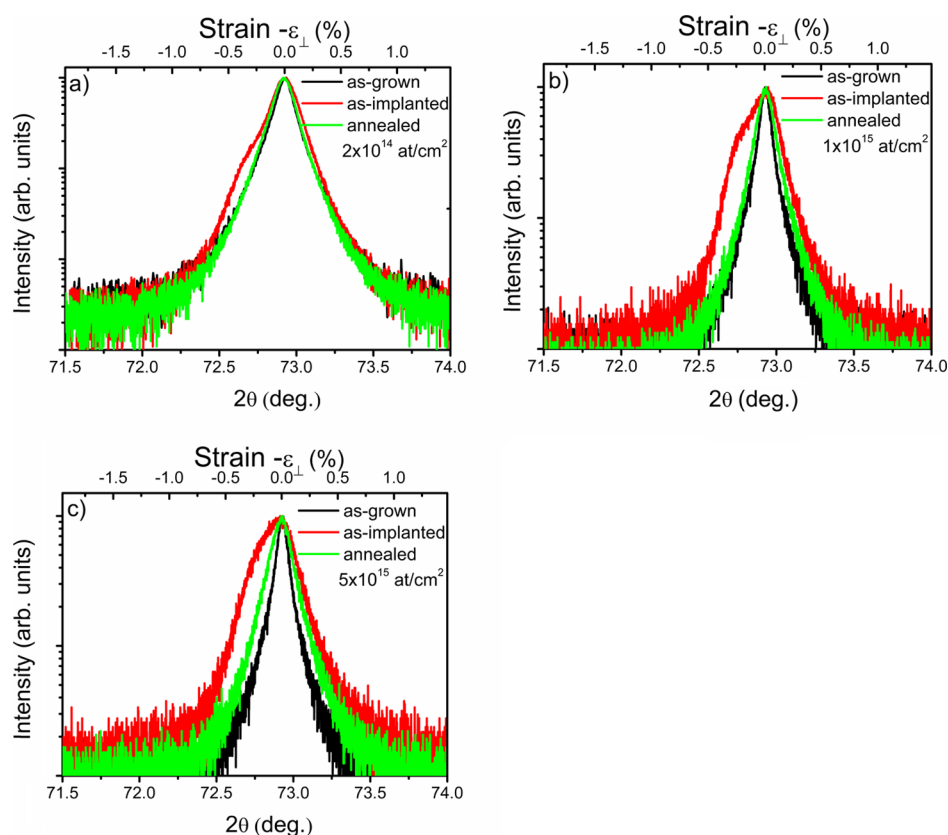


**Figure 6.** XRD  $2\theta$ - $\theta$  curves of high-density GaN NWs implanted with  $40^\circ$  tilt comparing as-grown, as-implanted, and annealed samples implanted to fluences of (a)  $2 \times 10^{14}$ , (b)  $1 \times 10^{15}$ , and (c)  $5 \times 10^{15}$  at./cm $^2$ .

for Eu implantation along the  $c$ -axis of GaN, except that the saturation regime, when the diffraction pattern does not evolve further, is only reached at higher fluences ( $1 \times 10^{15}$  at./cm $^2$ ).<sup>41</sup> This saturation was attributed to the formation of a dense network of extended defects leading to plastic deformation and strain relaxation. Many authors have reported similar strain formation in GaN for different implantation conditions.<sup>42–44</sup> In fact, it was suggested that strain induced by implantation defects is the driving force behind the defect mobility and dynamic annealing in GaN, leading to the change of defect microstructure as the fluence increases.<sup>45</sup> Detailed XRD studies on GaN NWs and NW heterostructures showed that, due to their vertical alignment, NWs can be studied by laboratory XRD in a similar way as planar heterostructures.<sup>46,47</sup> However, the diffraction intensity is strongly reduced due to the reduced sample volume and the fact that, due to the relatively high tilt between NWs, only a fraction of them will be well-oriented to satisfy the Bragg condition and contribute to the Bragg peak intensity. Moreover, the line shape and broadening are influenced by the inclination of the NWs normal to the scattering plane and inhomogeneous fluctuating strain.<sup>47</sup> Indeed, the XRD patterns of the as-grown NWs (see Figure 5a) show the typical non-Gaussian peak broadening, which Kaganer et al. attributed to random distortions caused by lattice defects at the interface between the NWs and the substrate and at joints between coalesced NWs.<sup>47</sup> Nevertheless, similar to the layers, a second peak formed after implantation is clearly visible, which is strongly overlapped to the Bragg peak arising from unimplanted GaN. Two main differences can be pointed out when comparing these diffraction patterns to those of the thin film reference samples.

First, the satellite peaks in NWs have a comparable intensity as the peak corresponding to unimplanted volume. This can be understood by the fact that the ratio of implanted/unimplanted volume in the NWs is much larger since not only a thin surface layer is doped but ions can enter through the side facets of the wires and penetrate the entire wire width. Like this, only the bases of the NWs remain unimplanted due to shadowing by the surrounding NWs. It is worth mentioning that we did not see any significant difference in the XRD patterns from the wafer center or the peripheries, suggesting that the 2D layer present in sample set 1 has a similar behavior as the NWs. Second and more importantly, the maximum strain that is reached is much lower in the NWs than in the thin films (see upper  $x$ -axis in Figure 5, where the angle was converted to perpendicular strain as  $\epsilon^\perp = (c_{\text{exp}} - c_0)/c_0$ , with  $c_0$  the  $c$ -lattice parameter of the as-grown GaN and  $c_{\text{exp}}$  the expanded  $c$ -lattice parameter as determined from the  $2\theta$  position of the XRD curves). While in thin films already for the lowest fluence the incorporated perpendicular strain exceeds 0.5%, this value is never reached in the NWs even for the highest investigated fluence. The lower strain state in NWs can be attributed to more efficient relaxation mechanisms in low-dimensional structures especially since implantation defects in NWs are expected to accumulate at the surface. The higher vacancy concentration (relative to interstitial defects) suggested by molecular dynamics simulations may also play a role.<sup>24</sup> Furthermore, it is possible that a biaxial component of defect-induced strain increases the perpendicular strain in bulk material due to the in-plane stress imposed by the unimplanted bulk,<sup>48</sup> while in NWs the  $a$ -lattice parameter is freer to expand. Strain in the  $c$ -plane is indeed predicted to occur by molecular

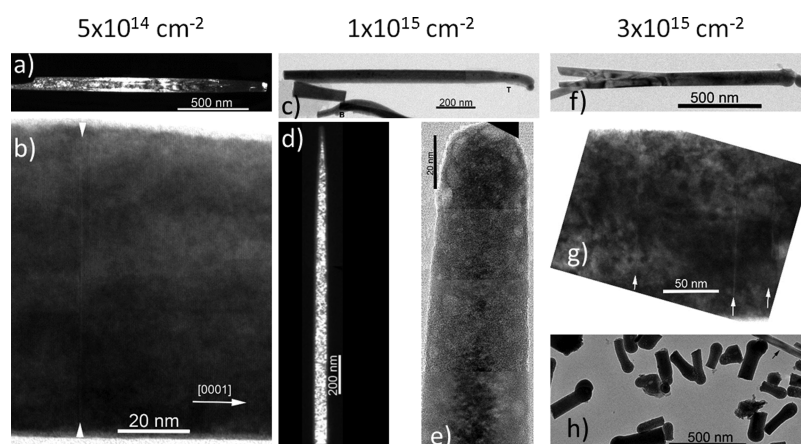


**Figure 7.** TEM images of as-implanted NWs implanted to a fluence of (a,b)  $5 \times 10^{14}$ , (c–e)  $1 \times 10^{15}$ , and (f–h)  $3 \times 10^{15}$   $\text{cm}^{-2}$ . Basal stacking faults are marked by white arrows.

dynamics simulations although with lower magnitude than the perpendicular strain.<sup>24</sup> Unfortunately, it was not possible to measure the  $a$ -lattice constant in the present work due to the small material volume in NW samples and the low intensity of the asymmetric XRD reflections. Synchrotron diffraction measurements should be done to clarify this point.

The effect of annealing on XRD  $2\theta$ – $\theta$  curves is shown in Figure 6 for the NW samples implanted with  $40^\circ$  tilt and annealed at  $1000^\circ\text{C}$ . In agreement with the Monte Carlo simulations showing that only the upper part of the NWs is implanted in this geometry, the intensity ratio of the diffraction peaks corresponding to implanted and virgin material is lower than for sample set 1. After annealing, the curves become symmetric and resemble those of the as-grown samples, suggesting that the defect induced strain is efficiently removed even for the highest fluence of  $5 \times 10^{15}$   $\text{at./cm}^2$ . Although direct comparison of the curves should be done with caution due to lateral inhomogeneities of the samples, a slight broadening of the curves for the annealed NWs implanted to the highest fluences is probably due to remaining implantation defects and surface degradation.

For thin film samples, efficient strain recovery is only seen for the lowest fluence of  $1 \times 10^{13}$   $\text{at./cm}^2$ ; for higher fluences, it is not even achieved after annealing at  $1450^\circ\text{C}$  as reported previously and diffraction curves remain asymmetric after annealing.<sup>32,49</sup>

There is no significant difference between the XRD results on samples implanted with  $20^\circ$  and  $40^\circ$  tilt. We recently showed that the defect structures in thin films strongly depend on the surface orientation ( $a$ -plane,  $c$ -plane, or  $m$ -plane);<sup>50</sup> however, the influence of the exact implantation geometry and its impact on damage in NWs needs further investigations.

The morphology changes upon implantation were investigated by TEM for the different fluences. Up to a fluence of  $5 \times 10^{14}$   $\text{at./cm}^2$ , no significant change has been noticed in the NW morphology (Figure 7a). All the NWs exhibit well-defined clean facets and no amorphization. Their diameter progressively decreases toward the top, which is probably due to the growth process. At this fluence, the NW may exhibit one or two basal stacking faults<sup>51</sup> across the entire width (marked with white arrows in Figure 7b). Such defects are probably generated by the ion implantation; indeed, they are known to constitute the basic deformation channel for GaN thin films during such an implantation process.<sup>19</sup> By the fluence of  $1 \times$

$10^{15}$   $\text{at./cm}^2$ , two types of structural changes are seen to take place in the NWs. As can be seen in Figure 7c, NWs can bend at the level of the tip (T), but also at their base (B), and this can be accompanied by rounding at the tips. However, at this fluence, most of the observed NWs stay upright as shown by the weak beam image recorded with  $g = 0002$  (Figure 7d). The exhibited contrast indicates that, although the NW has been damaged, the core retains a crystalline structure, all along the NW. This is also visible through the lattice fringes which disappear toward the outer part of the wire, which then displays a random contrast, indicating that this area has undergone amorphization. This is in contrast with our earlier reports on bulk GaN where up to the highest fluences the material was shown to transform to nanocrystalline form instead of becoming amorphous under ion implantation.<sup>52</sup> For this fluence and beyond, the formation of surface defects such as blisters (Figure 7e) is consistent with the high sputtering yields suggested by molecular dynamics simulations<sup>24</sup> and previous experimental results.<sup>22</sup> For the highest fluence ( $3 \times 10^{15}$   $\text{at./cm}^2$ ), only a limited number of NWs retain their integrity when transferred to the TEM grid for observation (Figure 7f); in this case the rounding of the tips is more prominent and more stacking faults can be seen in the less damaged parts of the NWs (Figure 7g). Nevertheless, compared to GaN epitaxial layers, the density of stacking faults is very small, which means that the formation of such defects is not the dominant mechanism in these low-dimensional structures. At this fluence, most of the NWs become brittle leading to the easy breaking-off of the top, which is the most sollicitated part of the NWs when they are transferred to the TEM grid (Figure 7h).

After annealing at  $1000^\circ\text{C}$ , STEM HAADF was carried out as shown in Figure 8 for a NW implanted with  $1 \times 10^{15}$   $\text{at./cm}^2$ . As can be seen in Figure 8a, the NW surface is no longer limited by large and regular crystallographic faces. In this low-magnification micrograph, the roughness is clearly visible on the sides and influences the contrast of the whole image as indicated by the darker spots, which reveal that the corresponding thickness is smaller than that of the surrounding areas. Most interesting, as shown in Figure 8b, the amorphous parts as well as the surface blisters have completely disappeared, which means that the amorphous areas may have recrystallized during the annealing process or evaporated. All along the annealed NW, no basal stacking faults can be seen

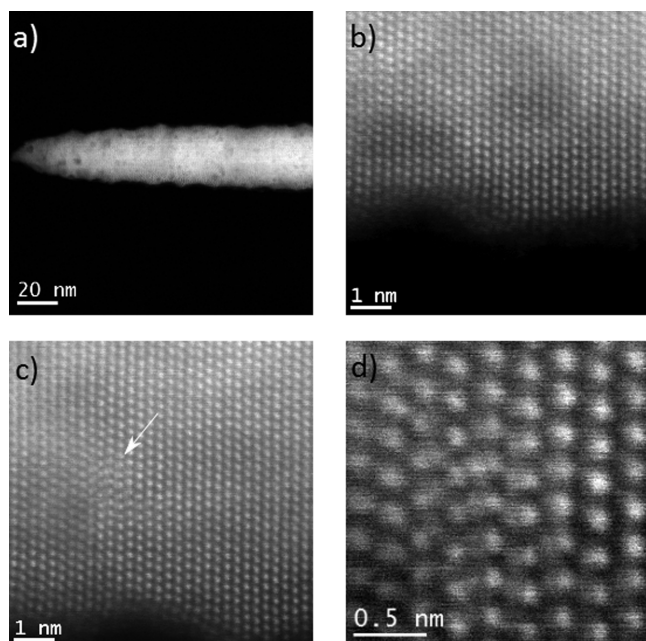


**Figure 8.** (a) STEM HAADF image of a NW implanted to a fluence of  $1 \times 10^{15}$  at./cm<sup>2</sup> and annealed at 1000 °C. (b–d) High-resolution STEM HAADF images of the same NW showing (b) high crystalline quality of the NW core and (c,d) isolated extended defect.

anymore, which is an indication that they have been removed. Only in very few areas, however, some local irregular features have been noticed (Figure 8c,d), which may correspond to small extended defects possibly consisting of three extra planes. This behavior is still under investigation.

**3.3. Optical Activation.** Despite the pronounced surface degradation but consistent with the high crystalline quality of the NW core, where most of the Eu ions should come to rest, all samples show optical activation of the Eu<sup>3+</sup> ions with the dominant line, corresponding to the <sup>5</sup>D<sub>0</sub> → <sup>7</sup>F<sub>2</sub> transition, at ~622 nm. The inset in Figure 9b presents the CL spectra of a NW and a thin film sample both implanted to a fluence of  $1 \times 10^{14}$  at./cm<sup>2</sup>. The spectra are representative for all fluences and confirm that the Eu<sup>3+</sup> optically active centers are similar in NWs and thin films. This is in agreement with the detailed photoluminescence (PL) spectroscopy study performed on a sub-set of the samples studied here and which showed that the dominant Eu<sup>3+</sup> center is the same in NWs and films, despite a small shift in the line positions presumably due to different strain states of the GaN hosts.<sup>8</sup> These observations were

independent of implantation fluence and geometry. In the following, we focus on the emission intensity. The CL intensity of the main Eu<sup>3+</sup> emission line at 622 nm is plotted in Figure 9 for NWs (a) and thin films (b) as a function of the fluence. The values were achieved by measuring three spectra in different points of the sample, which varied only slightly, and averaging the measured intensities. For the NW sample, this was done in two regions with high and low NW density. For the case of the doped thin films (Figure 9b), the intensity first increases with the fluence up to  $5 \times 10^{14}$  at./cm<sup>2</sup> and then decreases again due to the severe lattice damage which could not be removed by thermal annealing. This behavior is similar to that observed previously for implantations performed along the *c*-axis. However, in the latter case, the decrease of intensity only occurs at higher fluences,<sup>53</sup> which can be attributed to the lower damage level when implantation is performed in channeling geometry (which promotes the steering of ions along the atomic rows and reduces the direct collisions with the target nuclei).<sup>42,54</sup> For the case of the NWs, distinct behaviors are observed for regions with high or low NW density. For low NW density, a saturation of the emission for high fluences is observed. Although no pronounced intensity decrease occurs as for the thin films, the similar behavior might suggest that a large fraction of Eu was implanted into the 2D layer at the base of the NWs and with a similar behavior as that observed for thin films. For high NW density, on the other hand, no saturation or quenching is observed up to the highest measured fluence. However, the increase of emission intensity is much lower than expected when assuming a direct proportionality between Eu concentration and emission intensity. This implies that most of the implanted Eu ions in high fluence samples are not optically active. This can be either due to a less effective energy transfer from the GaN host to the Eu<sup>3+</sup> ions, the quenching of luminescence due to the formation of defects acting as nonradiative recombination centers or due to the incorporation of Eu in inadequate lattice sites, for example sites which do not support the 3+ valence state of the Eu ions.

In order to get a more microscopic view of Eu incorporation in NWs, nano-CL was performed on single NWs as presented in Figure 10. Figure 10a shows the CL spectra acquired at different positions along the NW length in the seven regions indicated in the TEM image of Figure 10b. Eu emission at 622 nm is clearly observed within the first 1000 nm from the top. This is in good agreement with the Monte Carlo simulations showing that most Eu ions come to rest in this region for high NW density. At the bottom part of the NW, only broader

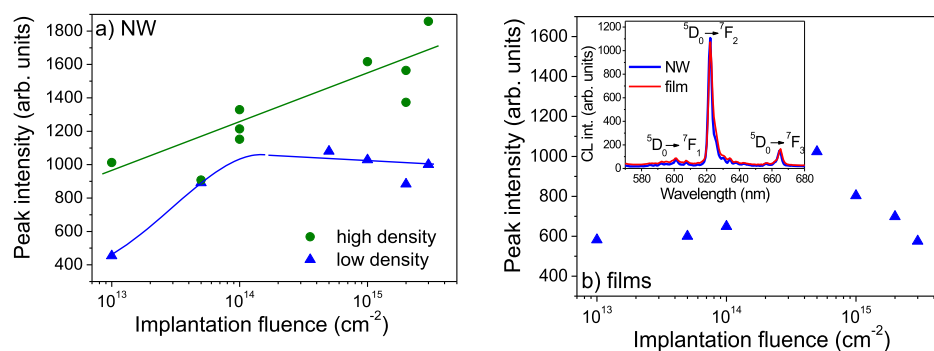


**Figure 9.** RT CL peak intensity of the Eu<sup>3+</sup> emission line at ~622 nm as a function of the fluence for NWs in regions with low and high NW density (a) and thin film reference samples (b). The inset in (b) compares typical CL spectra for NW and thin film samples.

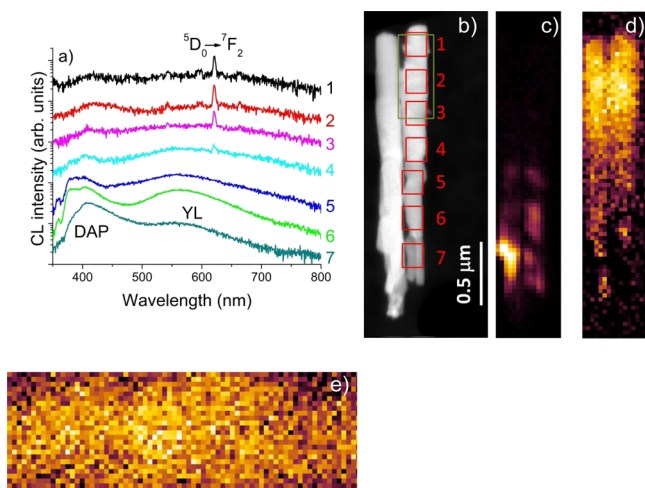


**Figure 10.** (a) Nano-CL spectra taken at seven points from the top (1) to the bottom (7) of a single NW implanted to a fluence of  $1 \times 10^{14}$  at./cm $^2$  ( $20^\circ$  incidence angle) and annealed at  $1000^\circ\text{C}$ . The regions at which the spectra were taken are indicated with red rectangles in (b). (c,d) Luminescence intensity maps integrating the spectra in a wavelength region from 350 to 550 nm (c) and around the 622 nm  $\text{Eu}^{3+}$  line (d). (e) Detail of the luminescence intensity map integrating the  $\text{Eu}^{3+}$  emission peak at 622 nm in the region with highest Eu-emission marked with the bigger green rectangle in (b); the pixel size is  $10 \times 10 \text{ nm}^2$ .

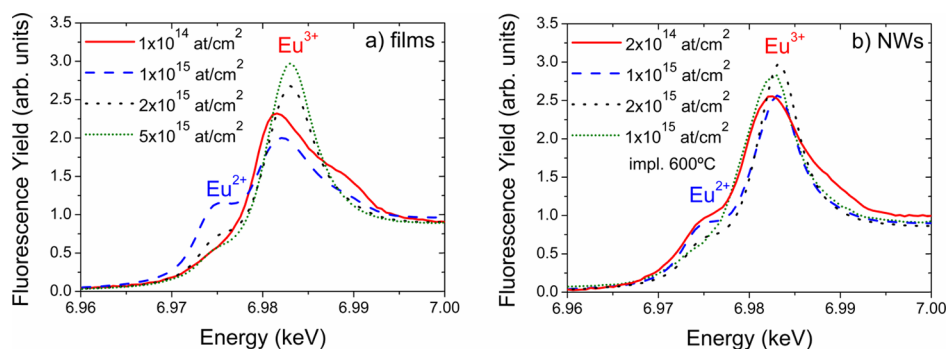
bands at  $\sim 400$  and  $\sim 570$  nm are observed. Emission at 400 nm was also observed in PL spectra of the as-grown samples and attributed to donor acceptor pair transitions, while the yellow emission was formed after implantation/annealing and attributed to defects.<sup>8</sup> In the present case, the yellow luminescence in spectra 5, 6, and 7 may be due to defects created by sputtered atoms or surface defects created during annealing. Figure 10c,d shows maps of the luminescence intensity from the same NW integrating the region from 350 to 550 nm (Figure 10c), corresponding mainly to DAP emission, and integrating only the  $\text{Eu}^{3+}$  emission line at 622 nm (Figure 10d). These maps clearly show that Eu-emission is mainly observed at the top of the NWs. Figure 10e presents a more detailed luminescence map of the  $\text{Eu}^{3+}$  emission within a region corresponding to the highest Eu concentration (marked with the larger green rectangle in Figure 10b). Lower  $\text{Eu}^{3+}$  emission intensity is observed at the NW edges due to both a lower probed sample volume and low Eu concentration at the surface. Even when disregarding the edges,  $\text{Eu}^{3+}$  emission

intensity fluctuations at the nanoscale are visible. Each pixel in the map corresponds to an area of  $10 \times 10 \text{ nm}^2$ . Taking into account, the NW density, dimension, and the fluence, the number of Eu ions can be roughly estimated to be some tens of ions per pixel. The spatial fluctuations of emission intensity can be explained by the facts that only a small fraction of Eu ions are optically active<sup>55,56</sup> as well as by the long lifetimes of the excited  $\text{Eu}^{3+}$  states leading to a long “dark-time” of individual ions. Furthermore, as mentioned above, ions may be incorporated into sites which do not promote optical activity for example due to a valence state different from  $3+$ .

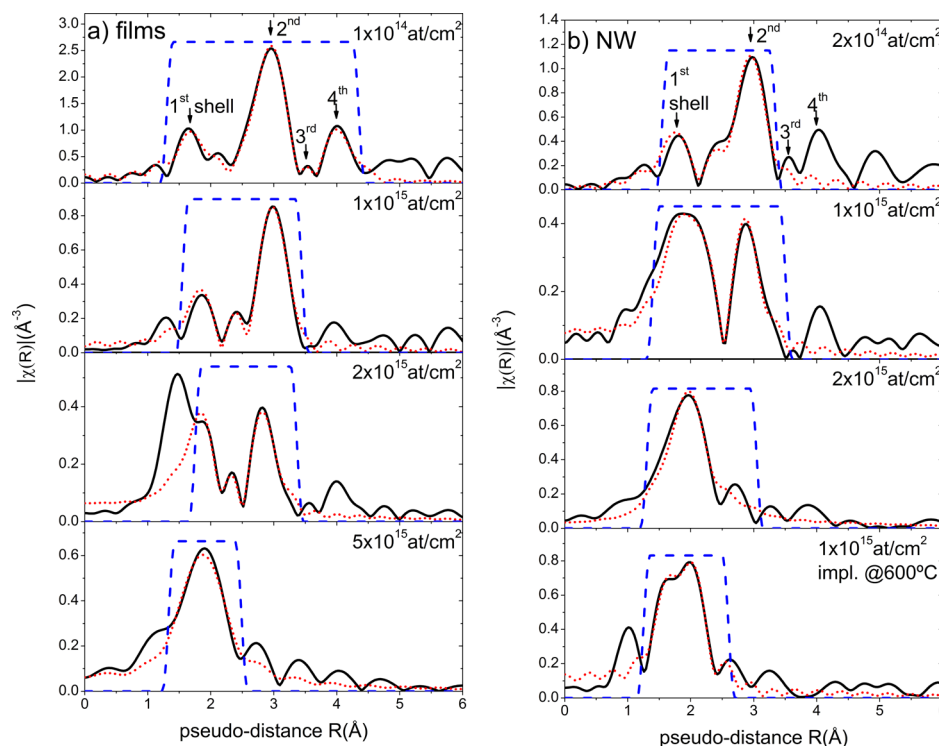
**3.4. Eu Incorporation.** Eu and other rare earth ions in GaN thin films are known to be preferentially incorporated in substitutional Ga-sites or slightly displaced from that site.<sup>6,55,57–60</sup> Experimentally, this was shown by ion channeling or emission channeling techniques, which cannot be easily applied to NWs due to the low critical angles for dechanneling which are in the order of the tilt angles between individual NWs. Therefore, here we apply X-ray absorption techniques to assess the incorporation site and valence state of implanted Eu ions in NWs and thin films. Indeed, EXAFS has been successfully applied in Eu implanted and in situ doped GaN films.<sup>61,62</sup> The nanoscopic nature of X-ray absorption techniques, being sensitive only to a few atomic neighbor shells around the probe atom, is ideal for the comparison of bulk material and nanostructures. A more detailed description of the data analysis can be found in the [Supporting Information](#).

Figure 11 presents the absorption spectra near the Eu  $L_{III}$  edge [X-ray absorption near-edge structure (XANES) part only] for various thin film (Figure 11a) and NW (Figure 11b) samples after annealing. All spectra exhibit two contributions to the absorption edge corresponding to the  $\text{Eu}^{2+}$  white line at fixed energy position  $6975.3 \pm 0.3$  eV, while the line for  $\text{Eu}^{3+}$  varies from 6981.5 to 6983.1 eV. This is most visible for the thin film sample implanted with a fluence of  $1 \times 10^{15}$  at./cm $^2$  (RTA at  $1000^\circ\text{C}$ ) with  $\text{Eu}^{2+}$  and  $\text{Eu}^{3+}$  fractions of 33 and 67%, respectively. Coexistence of Eu in 2+ and 3+ oxidation states has also been reported for Eu-doped ZnO NWs.<sup>63</sup> In contrast to GaN, in the case of ZnO, substitutional Eu is expected to reside in the 2+ charge state but interaction with intrinsic defects allows the stabilization in the 3+ charge state.<sup>64,65</sup>

We observe that the  $\text{Eu}^{2+}$  contribution decreases when the fluence is lowered to  $5 \times 10^{14}$  at./cm $^2$  and becomes hardly visible for the HTHP annealed reference sample implanted to a fluence of  $1 \times 10^{14}$  at./cm $^2$ , which shows an  $\text{Eu}^{2+}$  fraction of



**Figure 11.** XANES spectra for selected thin films (a) and NWs (b) showing the coexistence of Eu in the 2+ and 3+ charge state and the possibility of decreasing the  $\text{Eu}^{2+}$  fraction by HTHP annealing or implantation at elevated temperature plus RTA at  $1000^\circ\text{C}$ . The  $\text{Eu}^{2+}$  edge is found at a fixed position in all samples while the position of the  $\text{Eu}^{3+}$  varies slightly for different implantation/annealing conditions.



**Figure 12.** Fourier transform of the EXAFS signal and fits of selected films (a) and NWs (b) showing the experimental data (black solid line), the fit (red dotted line) and the window used to do the fit (blue dashed line). Note that in thin film sample  $2 \times 10^{15}$  at./cm<sup>2</sup>, the low- $R$  bump is an artifact arising from a baseline residual oscillation that could not be suppressed.

only 16%. A low  $\text{Eu}^{2+}$  fraction of 18% is also seen for NW samples implanted to a fluence as high as  $1 \times 10^{15}$  at./cm<sup>2</sup>, provided they are implanted at 600 °C. As the high implantation temperature promotes defect mobility during the implantation, this can lead to annihilation of defects or to increased interaction of defects among each other.

XANES measurements for Eu implanted directly in Si, SiO<sub>2</sub>, and Si<sub>3</sub>N<sub>4</sub> wafers revealed that Eu in these materials is incorporated entirely in the 2+ charge state (see Supporting Information); as implantation of GaN NWs at 600 °C results in more than 80% of  $\text{Eu}^{3+}$ , this is coherent with nano-CL results which suggested that Eu does not reach the Si substrate. Consequently, the presence of  $\text{Eu}^{2+}$  in GaN seems to be correlated with the presence of residual implantation defects after annealing.

However, the correlation of defect density and  $\text{Eu}^{2+}$  fraction is not straightforward. As can be seen in Figure 11a,b, the  $\text{Eu}^{2+}$  fraction is decreasing with further increase of fluence above  $1 \times 10^{15}$  at./cm<sup>2</sup> for both NW and thin film samples, although the residual defect density should be higher for these high fluence implantations. This complex behavior shows that not simply the overall defect concentration is decisive for the Eu charge state but also the exact defect arrangement and nature around the Eu ion.

It is interesting to mention that the irradiation of as-implanted (not annealed) samples with X-rays leads to the photo-oxidation of  $\text{Eu}^{2+}$  to  $\text{Eu}^{3+}$ , which induced an  $\text{Eu}^{3+}/\text{Eu}^{2+}$  ratio increase of up to 40% in 7 h (see Supporting Information for further details). For the highest fluence of  $5 \times 10^{15}$  at./cm<sup>2</sup>, directly after the implantation, the fraction of  $\text{Eu}^{2+}$  is as high as 31% for thin films and 44% for NWs and reduces after annealing to 13 and 22%, respectively. Analogously, thermal annealing leads to conversion of  $\text{Eu}^{2+}$  to  $\text{Eu}^{3+}$ . The increasing

$\text{Eu}^{3+}/\text{Eu}^{2+}$  ratio, caused either by thermal annealing or X-ray irradiation, is accompanied by a better-defined EXAFS signal revealing a more ordered environment around Eu suggesting annealing of defects. Therefore, we concentrated our further investigation on annealed samples, where, within the duration of the EXAFS measurement, no changes were seen for the case of NWs and only moderate changes for thin film samples.

Inspecting the shape of the XANES curves in Figure 11, there is a clear evolution when decreasing the implantation fluence with a shift of the  $\text{Eu}^{3+}$  absorption edge to a lower energy and a third feature occurring at the high energy side of the  $\text{Eu}^{3+}$  white line. Such a change is most likely related with a local change of the Eu nearest neighbors' coordination. This interpretation is also supported by the EXAFS results shown in Figure 12 (for a detailed description of the EXAFS data analysis see the Supporting Information).

Figure 12 shows the Fourier transforms of the EXAFS spectra and fits for NW and thin film samples implanted to different fluences after annealing at 1000 °C as well as the thin film reference after HTHP annealing at 1400 °C. Qualitatively, the results are very similar for NWs and thin films. For the highest fluence, only the first neighbor shell (lowest  $R$  bump around pseudo-radius  $R = 2$  Å) is visible and corresponds to light atoms, presumably nitrogen. The second neighbor shell (expected around pseudo-radius  $R = 3$  Å) is not visible, suggesting that Eu and N in the first shell form a locally ordered complex while the distortion of the crystal due to the oversized Eu (compared to Ga) and due to implantation defects prevents a well-ordered crystal structure of the second shell and beyond. With decreasing fluence and therefore decreasing defect density, intensity of the first shell decreases, that is the number of N atoms in the first neighbor shell is reduced, while the second neighbor shell intensity—consisting

of Ga atoms—becomes increasingly visible thus revealing the ordering of the crystal structure around Eu.

Detailed data fitting allows further interpretation of this data. Starting with the low fluence HTHP annealed reference layer, the  $|\chi(R)|$  graph (see Figure 12a) reveals at least eight well-defined surrounding shells below 6 Å with a maximal intensity on the second shell at pseudo-radius  $R = 3$  Å. This demonstrates that the Eu local environment is of very good crystalline quality, dominated by a second shell of heavy elements. A good fit is obtained assuming 100% of the Eu incorporated on substitutional Ga-sites, that is with 4 nitrogen atoms as nearest neighbors, 12 Ga-atoms in the second, 10 N-atoms in the third, and 6 Ga atoms in the fourth neighbor shells. The first neighbor shell is strongly distorted (by  $\sim 11\%$  with an Eu–N nearest neighbor distance of 2.15 Å compared to a Ga–N nearest neighbor distance of 1.94 Å in pure GaN) as expected, due to the large effective ionic radius of  $\text{Eu}^{3+}$  (linearly estimated to 83.5 pm) compared to  $\text{Ga}^{3+}$  (61 pm) in tetrahedral environment<sup>66</sup> and in good agreement with previous studies on rare earth-doped GaN and other III–N alloys.<sup>61,62,67,68</sup> The more distant shells are found close to the expected positions in undisturbed GaN (with a Eu–Ga next-nearest neighbor distance of 3.17 Å compared to a Ga–Ga nearest neighbor distance of 3.18 Å in GaN). Debye–Waller factors are small ( $< 5 \times 10^{-3} \text{ \AA}^{-2}$  for all shells) revealing a good crystal quality. The strongly dilated first neighbor shell would allow for the incorporation of more than 4 nitrogen atoms and indeed leaving the number of next nearest neighbors as free fitting parameter yields  $5.3 \pm 1.9$  N as first shell without changing the goodness of the fit. It should be noted that a contribution of oxygen on the first nearest neighbor site cannot be discarded.

The graph for the lowest fluence in NWs looks qualitatively similar (see Figure 12b) but cannot be fitted assuming 100% of undisturbed substitutional Eu. The simplest model able to satisfactorily fit the data of all samples consists of two fractions of Eu: the first fraction corresponding to undisturbed substitutional sites,  $\text{Eu}_{\text{Ga}}$ , and the second fraction (dominant for higher fluences and in the following named EuN-like fraction) characterized by a local arrangement consisting of more than 4 nitrogen atoms at a distance of  $\sim 2.5$  Å, that is considerably larger than for  $\text{Eu}_{\text{Ga}}$  but similar to the Eu–N distance in EuN which is 2.51 Å.<sup>69</sup> Details of the fit results are given in the Supporting Information. The main conclusion is illustrated in Figure 13, showing the fraction of substitutional  $\text{Eu}_{\text{Ga}}$  as a function of the fluence for all analyzed samples. The substitutional fraction is seen to decrease with implantation fluence and is typically lower for NW samples than for thin film samples. For the highest fluence in thin films and NWs, this fraction approaches zero and all Eu ions are found in EuN-like environment. The figure shows furthermore that the as-implanted NWs ( $1 \times 10^{15} \text{ at./cm}^2$ ) show slightly higher substitutional fractions than after annealing which is consistent with ion channeling data on ion-implanted thin films and probably due to defect diffusion and trapping during annealing.<sup>53</sup>

Although the  $1 \times 10^{15} \text{ at./cm}^2$  (RTA@1000 °C) NW sample implanted at 600 °C reveals a higher  $\text{Eu}^{3+}/\text{Eu}^{2+}$  ratio than for implantation at room temperature, the  $\text{Eu}_{\text{Ga}}$  substitutional fraction drops to zero. The higher mobility of defects during implantation at elevated temperatures seems to favor the formation of EuN-like complexes. This is consistent

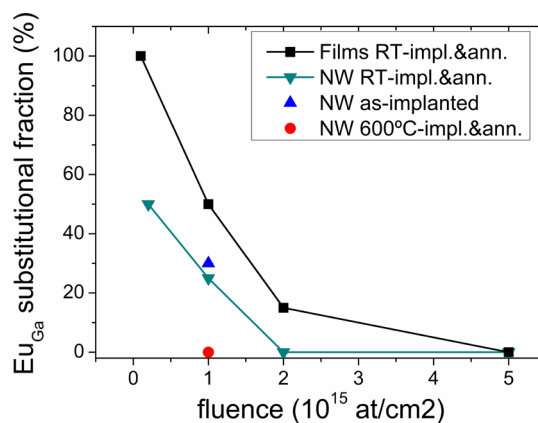


**Figure 13.** Fraction of Eu incorporated in substitutional Ga-sites as a function of the fluence for thin film and NW samples in different conditions as given in the legend. RT-impl.: implanted at RT; 600 °C-impl.: implanted at 600 °C; ann: annealed at 1000 °C except for the thin film sample implanted to  $1 \times 10^{14} \text{ at./cm}^2$  which was annealed at 1400 °C.

with the XANES spectral shape which resembles that of high fluence implanted samples (see Figure 11).

On first sight, the change of preferential incorporation site from  $\text{Eu}_{\text{Ga}}$  for low fluences to EuN-like for high fluences might seem contradicting to the optical data showing similar spectral shapes for all samples. This discrepancy shows once more that only a small fraction of Eu is optically active while in EXAFS we probe the majority sites. This interpretation is consistent with the slow increase/saturation of Eu-luminescence intensity in NWs and the decrease in thin films (see Figure 9).

#### 4. CONCLUSIONS

GaN NWs and thin films were implanted with Eu ions in a fluence range from  $1 \times 10^{13} \text{ at./cm}^2$  to  $5 \times 10^{15} \text{ at./cm}^2$ . The distribution of Eu inside the NWs can be tuned by adapting the NW diameter, density, and implantation conditions as shown by Monte Carlo simulations. Implantation damage was assessed by XRD revealing considerably lower strain introduced by implantation defects in NWs than in thin films implanted in the same condition. In good agreement, and despite a high level of surface defects, the NW core is shown to be of high crystal quality for fluences as high as  $1 \times 10^{15} \text{ at./cm}^2$  and after annealing. The formation of extended defects and defect clusters is suppressed compared with implantation studies in GaN thin films. Optical activation of  $\text{Eu}^{3+}$  is achieved upon annealing with similar optical centers in NWs and thin films. For the case of NWs, the CL emission intensity increases within the entire fluence range, while it saturates or even decreases at higher fluences for the case of thin films suggesting stronger luminescence quenching due to implantation defects in thin films. Eu ions coexist in 2+ and 3+ charge state although  $\text{Eu}^{2+}$  can be almost suppressed by optimizing the implantation and annealing conditions. The local lattice environment of Eu is similar in NWs and thin films; however, in both cases it is strongly distorted by implantation defects and the oversized Eu ion. In particular, for high fluences, EXAFS only shows a signal from the first neighbor shell and suggests that a large fraction of Eu resides in a EuN-like configuration. For lower fluences and more efficient annealing techniques, EXAFS results are consistent with a substitution of Ga by Eu. This transition from an EuN to a GaN:Eu<sub>Ga</sub>-like

structure occurs at lower fluences for NWs than for thin films, suggesting that the EuN-like structure forms more easily in NWs. The presented results help to establish guidelines for the use of ion implantation as a processing tool for GaN nanostructures. In particular, and despite the successful optical activation of Eu in all samples, high fluences should be avoided due to severe surface damage and the formation of local EuN-like structures.

## ■ ASSOCIATED CONTENT

### Supporting Information

The Supporting Information is available free of charge on the ACS Publications website at DOI: 10.1021/acs.jpcc.8b12014.

Details of the dynamic Monte Carlo simulation. Details on XAS analysis: Eu charge state in GaN and changes of the XANES signal with X-ray irradiation—Eu charge state in Si, SiO<sub>2</sub>, and Si<sub>3</sub>N<sub>4</sub>—EXAFS signal analysis (PDF)

XANES spectra taken consecutively on NWs implanted with  $5 \times 10^{15}$  at./cm<sup>2</sup> without annealing (PDF)

Fractions of Eu<sup>3+</sup> and Eu<sup>2+</sup> as a function of the X-ray irradiation time (PDF)

XANES spectra around the Eu L<sub>III</sub> edge in Eu-implanted and annealed (RTA 1000 °C) Si, SiO<sub>2</sub>, and Si<sub>3</sub>N<sub>4</sub> (TIF)

Amplitude of the Fourier transform of the  $k_2\chi(k)$  EXAFS spectrum (TIF)

Real part of the filtered back-Fourier transform (TIF)

## ■ AUTHOR INFORMATION

### Corresponding Author

\*E-mail: [lorenz@ctn.tecnico.ulisboa.pt](mailto:lorenz@ctn.tecnico.ulisboa.pt). Phone: +351-219946052. Fax: +351 21 9946285.

### ORCID

E. Nogales: 0000-0003-3376-6320

L. H. G. Tizei: 0000-0003-3998-9912

M. Kociak: 0000-0001-8858-0449

B. Méndez: 0000-0002-6289-7437

K. Lorenz: 0000-0001-5546-6922

### Present Address

<sup>○</sup>Departamento de Física Aplicada y Centro de Micro-Análisis de Materiales, Universidad Autónoma de Madrid, Madrid, Spain.

### Notes

The authors declare no competing financial interest.

## ■ ACKNOWLEDGMENTS

This work has been supported by the bilateral collaboration program Pessoa and the project NASIB funded by FCT and FEDER (PTDC/CTM-CTM/28011/2017, LISBOA-01-0145-FEDER-028011). M.P. acknowledges support by FCT Portugal through grant SFRH/BPD/111285/2015. B.M. and E.N. acknowledge support by MINECO (projects n° MAT 2015-65274-R-FEDER, n° MAT 2016-81720-REDC). A.R.C. acknowledges the grant by Ramón y Cajal programs (under contract number RYC-2015-18047). The research leading to these results has received funding from the European Union Seventh Framework Programme under grant agreement 312483—ESTEEM2 (Integrated Infrastructure Initiative-I3), the ITN project “Supporting Postgraduate Research with Internships in industry and Training Excellence (SPRITE)”, and the infrastructure project “Research And Development

with Ion Beams—Advancing Technology in Europe (RADIATE)”. We thank I. S. Roqan (KAUST, Saudi Arabia) for the MOCVD GaN reference layers, M. Boćkowski (Unipress, Poland) for the HTHP annealing of the thin film reference sample, and I. Kieffer (FAME beamline, ESRF, France) and E. Salas-Colera (SPLINE beamline, ESRF, France) for their help in recording good-quality XAFS spectra and ESRF for the allocated beamtime (MA-2151, 30-02-1067, MA-2964).

## ■ REFERENCES

- (1) *Rare-Earth Doped III-Nitrides for Optoelectronic and Spintronic Applications*; O'Donnell, K. P.; Dierolf, V., Eds.; Springer: Dordrecht, 2010.
- (2) Nishikawa, A.; Kawasaki, T.; Furukawa, N.; Terai, Y.; Fujiwara, Y. Room-temperature red emission from a p-type/europium-doped/n-type gallium nitride light-emitting diode under current injection. *Appl. Phys. Express* **2009**, *2*, 071004.
- (3) O'Donnell, K. P.; Auf der Maur, M.; Di Carlo, A.; Lorenz, K. It's not easy being green: Strategies for all-nitrides, all-colour solid state lighting. *Phys. Status Solidi RRL* **2012**, *6*, 49–52.
- (4) Steckl, A. J.; Heikenfeld, J. C.; Lee, D.-S.; Garter, M. J.; Baker, C. C.; Wang, Y.; Jones, R. Rare-Earth-Doped GaN: Growth, properties, and fabrication of electroluminescent devices. *IEEE J. Sel. Top. Quantum Electron.* **2002**, *8*, 749–766.
- (5) Lozykowski, H. J.; Jadwisienczak, W. M.; Brown, I. Visible cathodoluminescence of GaN doped with Dy, Er, and Tm. *Appl. Phys. Lett.* **1999**, *74*, 1129–1131.
- (6) Alves, E.; Lorenz, K.; Vianden, R.; Boemare, C.; Soares, M. J.; Monteiro, T. Optical doping of nitrides by ion implantation. *Mod. Phys. Lett. B* **2001**, *15*, 1281–1287.
- (7) Xu, C.; Chun, J.; Chon, B.; Joo, T.; Kim, D. E. In situ fabrication and blueshifted red emission of GaN:Eu nanoneedles. *Nanotechnology* **2007**, *18*, 015703.
- (8) Rodrigues, J.; Leitão, M. F.; Carreira, J. F. C.; Sedrine, N. B.; Santos, N. F.; Felizardo, M.; Auzelle, T.; Daudin, B.; Alves, E.; Neves, A. J.; et al. Spectroscopic analysis of Eu<sup>3+</sup> implanted and annealed GaN layers and nanowires. *J. Phys. Chem. C* **2015**, *119*, 17954–17964.
- (9) Sekiguchi, H.; Nishikawa, S.; Imanishi, T.; Ozaki, K.; Yamane, K.; Okada, H.; Kishino, K.; Wakahara, A. Structural and optical properties of Eu-doped GaN nanocolumns on (111) Si substrates grown by RF-plasma-assisted molecular beam epitaxy. *Jpn. J. Appl. Phys.* **2016**, *55*, 05FG07.
- (10) Consonni, V. Self-induced growth of GaN nanowires by molecular beam epitaxy: A critical review of the formation mechanisms. *Phys. Status Solidi RRL* **2013**, *7*, 699–712.
- (11) Aravindh, S. A.; Roqan, I. S. Defect-impurity complex induced long-range ferromagnetism in GaN nanowires. *Mater. Res. Express* **2015**, *2*, 126104.
- (12) Woodward, N.; Nishikawa, A.; Fujiwara, Y.; Dierolf, V. Site and sample dependent electron-phonon coupling of Eu ions in epitaxially-grown GaN layers. *Opt. Mater.* **2011**, *33*, 1050–1054.
- (13) Bodiou, L.; Braud, A.; Doualan, J.-L.; Moncorgé, R.; Park, J. H.; Munasinghe, C.; Steckl, A. J.; Lorenz, K.; Alves, E.; Daudin, B. Optically active centers in Eu implanted, Eu in situ doped GaN, and Eu doped GaN quantum dots. *J. Appl. Phys.* **2009**, *105*, 043104.
- (14) Rodrigues, J.; Ben Sedrine, N.; Felizardo, M.; Soares, M. J.; Alves, E.; Neves, A. J.; Fellmann, V.; Tourbot, G.; Auzelle, T.; Daudin, B.; et al. GaN:Pr<sup>3+</sup> nanostructures for red solid state light emission. *RSC Adv.* **2014**, *4*, 62869.
- (15) Ronning, C.; Borschel, C.; Geburt, S.; Niepelt, R. Ion beam doping of semiconductor nanowires. *Mater. Sci. Eng. R* **2010**, *70*, 30–43.
- (16) Fukata, N.; Takiguchi, R.; Ishida, S.; Yokono, S.; Hishita, S.; Murakami, K. Recrystallization and reactivation of dopant atoms in ion-implanted silicon nanowires. *ACS Nano* **2012**, *6*, 3278–3283.
- (17) Kucheyev, S. O.; Williams, J. S.; Pearton, S. J. Ion implantation into GaN. *J. Mater. Sci. Eng.* **2001**, *33*, 51–108.

- (18) Lorenz, K.; Peres, M.; Franco, N.; Marques, J. G.; Miranda, S. M. C.; Magalhães, S.; Monteiro, T.; Wesch, W.; Alves, E.; Wendler, E. Radiation damage formation and annealing in GaN and ZnO. *Proceedings of SPIE*, 2011; Vol. 7940, p 79400O.
- (19) Ruterana, P.; Lacroix, B.; Lorenz, K. A Mechanism for damage formation in GaN during rare earth ion implantation at medium range energy and room temperature. *J. Appl. Phys.* **2011**, *109*, 013506.
- (20) Turos, A. On the mechanism of damage buildup in gallium nitride. *Radiat. Eff. Defects Solids* **2013**, *168*, 431–441.
- (21) Dhara, S.; Datta, A.; Wu, C. T.; Lan, Z. H.; Chen, K. H.; Wang, Y. L.; Chen, L. C.; Hsu, C. W.; Lin, H. M.; Chen, C. C. Enhanced dynamic annealing in Ga<sup>+</sup> ion-implanted GaN nanowires. *Appl. Phys. Lett.* **2003**, *82*, 451–453.
- (22) Dhara, S.; Datta, A.; Wu, C. T.; Chen, K. H.; Wang, Y. L.; Muto, S.; Tanabe, T.; Shen, C. H.; Hsu, C. W.; Chen, L. C.; Maruyama, T. Mechanism of nanoblisters formation in Ga<sup>+</sup> self-ion implanted GaN nanowires. *Appl. Phys. Lett.* **2005**, *86*, 203119.
- (23) Lorenz, K.; Nogales, E.; Miranda, S. M. C.; Franco, N.; Méndez, B.; Alves, E.; Tourbot, G.; Daudin, B. Enhanced red emission from praseodymium-doped GaN nanowires by defect engineering. *Acta Mater.* **2013**, *61*, 3278–3284.
- (24) Ullah, M. W.; Kuronen, A.; Stukowski, A.; Djurabekova, F.; Nordlund, K. Atomistic simulation of Er irradiation induced defects in GaN nanowires. *J. Appl. Phys.* **2014**, *116*, 124313.
- (25) Bartels, J.; Freitag, K.; Marques, J. G.; Soares, J. C.; Vianden, R. Incorporation of the transition metal Hf into GaN. *Hyperfine Interact.* **1999**, *120–121*, 397–402.
- (26) Lorenz, K.; Wahl, U.; Alves, E.; Nogales, E.; Dalmaso, S.; Martin, R. W.; O'Donnell, K. P.; Wojdak, M.; Braud, A.; Monteiro, T.; et al. High temperature annealing of rare earth implanted GaN films: Structural and optical properties. *Opt. Mater.* **2006**, *28*, 750–758.
- (27) Roqan, I. S.; O'Donnell, K. P.; Martin, R. W.; Edwards, P. R.; Song, S. F.; Vantomme, A.; Lorenz, K.; Alves, E.; Boćkowski, M. Identification of the prime optical center in GaN:Eu<sup>3+</sup>. *Phys. Rev. B: Condens. Matter Mater. Phys.* **2010**, *81*, 085209.
- (28) Auzelle, T.; Haas, B.; Minj, A.; Bougerol, C.; Rouvière, J.-L.; Cros, A.; Colchero, J.; Daudin, B. The influence of AlN buffer over the polarity and the nucleation of self-organized GaN nanowires. *J. Appl. Phys.* **2015**, *117*, 245303.
- (29) Möller, W. TRI3DYN—Collisional computer simulation of the dynamic evolution of 3-dimensional nanostructures under ion irradiation. *Nucl. Instrum. Methods Phys. Res., Sect. B* **2014**, *322*, 23–33.
- (30) Möller, W.; Johannes, A.; Ronning, C. Shaping and compositional modification of zinc oxide nanowires under energetic manganese ion irradiation. *Nanotechnology* **2016**, *27*, 175301.
- (31) Berencén, Y.; Prucnal, S.; Möller, W.; Hübner, R.; Rebohle, L.; Böttger, R.; Glaser, M.; Schönherr, T.; Yuan, Y.; Wang, M.; Georgiev, Y. M.; Erbe, A.; Lugstein, A.; Helm, M.; Zhou, S.; Skorupa, W. CMOS-Compatible Controlled Hyperdoping of Silicon Nanowires. *Adv. Mater. Interfaces* **2018**, *5*, 1800101.
- (32) Lorenz, K.; Miranda, S. M. C.; Alves, E.; Roqan, I. S.; O'Donnell, K. P.; Boćkowski, M. High pressure annealing of Europium implanted GaN. *Proceedings of SPIE*, 2012; Vol. 8262, p 82620C.
- (33) Drouin, D.; Couture, A. R.; Joly, D.; Tastet, X.; Aimez, V.; Gauvin, R. CASINO V2.42-A fast and easy-to-use modeling tool for scanning electron microscopy and microanalysis users. *Scanning* **2007**, *29*, 92.
- (34) Zagonel, L. F.; Mazzucco, S.; Tencé, M.; March, K.; Bernard, R.; Laslier, B.; Jacopin, G.; Tchernycheva, M.; Rigutti, L.; Julien, F. H.; Songmuang, R.; Kociak, M. Nanometer scale spectral imaging of quantum emitters in nanowires and its correlation to their atomically resolved structure. *Nano Lett.* **2011**, *11*, 568–573.
- (35) Proux, O.; Nassif, V.; Prat, A.; Ulrich, O.; Lahera, E.; Biquard, X.; Menthonnex, J.-J.; Hazemann, J.-L. Feedback system of a liquid-nitrogen-cooled double-crystal monochromator: design and performances. *J. Synchrotron Radiat.* **2006**, *13*, 59–68.
- (36) Proux, O.; Biquard, X.; Lahera, E.; Menthonnex, J. J.; Prat, A.; Ulrich, O.; Soldo, Y.; Trivison, P.; Kapoujyan, G.; Perroux, G.; et al. FAME a new beamline for X-ray absorption investigations of very diluted systems of environmental, material and biological interests. *Phys. Scr.* **2005**, *115*, 970–973.
- (37) Rubio-Zuazo, J.; Collado-Negro, V.; Heyman, C.; Ferrer, P.; Silva, I. d.; Gallastegui, J. A.; Gutiérrez-León, A.; Castro, G. R. A double crystal X-ray monochromator for the SpLine diffraction and absorption synchrotron bending magnet beamline at the ESRF. *J. Phys.: Conf. Ser.* **2013**, *425*, 052005.
- (38) Ravel, B.; Newville, M. ATHENA, ARTEMIS, HEPHAESTUS: data analysis for X-ray absorption spectroscopy using IFEFFIT. *J. Synchrotron Radiat.* **2005**, *12*, 537–541.
- (39) Ren, W.; Kuronen, A.; Nordlund, K. Atomistic simulation of irradiation effects in GaN nanowires. *Nucl. Instrum. Methods Phys. Res., Sect. B* **2014**, *326*, 15–18.
- (40) Liu, C.; Mensching, B.; Volz, K.; Rauschenbach, B. Lattice expansion of Ca and Ar ion implanted GaN. *Appl. Phys. Lett.* **1997**, *71*, 2313–2315.
- (41) Lacroix, B.; Leclerc, S.; Declémy, A.; Lorenz, K.; Alves, E.; Ruterana, P. Mechanisms of damage formation in Eu-implanted GaN probed by X-ray diffraction. *Europhys. Lett.* **2011**, *96*, 46002.
- (42) Pipeleers, B.; Hogg, S. M.; Vantomme, A. Influence of the implantation angle on the generation of defects for Er implanted GaN. *Nucl. Instrum. Methods Phys. Res., Sect. B* **2003**, *206*, 95–98.
- (43) Faye, D. N.; Wendler, E.; Felizardo, M.; Magalhães, S.; Alves, E.; Brunner, F.; Weyers, M.; Lorenz, K. Mechanisms of implantation damage formation in Al<sub>x</sub>Ga<sub>1-x</sub>N compounds. *J. Phys. Chem. C* **2016**, *120*, 7277–7283.
- (44) Magalhães, S.; Fialho, M.; Peres, M.; Lorenz, K.; Alves, E. Quantitative x-ray diffraction analysis of bimodal damage distributions in Tm implanted Al<sub>0.15</sub>Ga<sub>0.85</sub>N. *J. Phys. D: Appl. Phys.* **2016**, *49*, 135308.
- (45) Pagowska, K.; Ratajczak, R.; Stonert, A.; Turos, A.; Nowicki, L.; Sathish, N.; Józwick, P.; Muecklich, A. RBS/Channeling and TEM study of damage buildup in ion bombarded GaN. *Acta Phys. Pol.* **2011**, *120*, 153.
- (46) Kaganer, V. M.; Wölz, M.; Brandt, O.; Geelhaar, L.; Riechert, H. X-ray diffraction profiles from axial nanowire heterostructures. *Phys. Rev. B: Condens. Matter Mater. Phys.* **2011**, *83*, 245321.
- (47) Kaganer, V. M.; Jenichen, B.; Brandt, O.; Fernández-Garrido, S.; Dogan, P.; Geelhaar, L.; Riechert, H. Inhomogeneous strain in GaN nanowires determined from x-ray diffraction peak profiles. *Phys. Rev. B: Condens. Matter Mater. Phys.* **2012**, *86*, 115325.
- (48) Debelle, A.; Declémy, A. XRD investigation of the strain/stress state of ion-irradiated crystals. *Nucl. Instrum. Methods Phys. Res., Sect. B* **2010**, *268*, 1460–1465.
- (49) Miranda, S. M. C.; Edwards, P. R.; O'Donnell, K. P.; Boćkowski, M.; Alves, E.; Roqan, I. S.; Vantomme, A.; Lorenz, K. Sequential multiple-step europium ion implantation and annealing of GaN. *Phys. Status Solidi C* **2014**, *11*, 253–257.
- (50) Lorenz, K.; Wendler, E.; Redondo-Cubero, A.; Catarino, N.; Chauvat, M.-P.; Schwaiger, S.; Scholz, F.; Alves, E.; Ruterana, P. Implantation damage formation in a-, c- and m-plane GaN. *Acta Mater.* **2017**, *123*, 177–187.
- (51) Potin, V.; Ruterana, P.; Potin, V.; Nouet, G. HREM study of stacking faults in GaN layers grown on sapphire substrate. *J. Phys.: Condens. Matter* **2000**, *12*, 10301–10306.
- (52) Gloux, F.; Wojtowicz, T.; Ruterana, P.; Lorenz, K.; Alves, E. Transmission electron microscopy investigation of the structural damage formed in GaN by medium range energy rare earth ion implantation. *J. Appl. Phys.* **2006**, *100*, 073520.
- (53) Lorenz, K.; Barradas, N. P.; Alves, E.; Roqan, I. S.; Nogales, E.; Martin, R. W.; O'Donnell, K. P.; Gloux, F.; Ruterana, P. Structural and optical characterization of Eu-implanted GaN. *J. Phys. D: Appl. Phys.* **2009**, *42*, 165103.
- (54) Lorenz, K.; Alves, E.; Gloux, F.; Ruterana, P.; Peres, M.; Neves, A. J.; Monteiro, T. Optical doping and damage formation in AlN by Eu implantation. *J. Appl. Phys.* **2010**, *107*, 023525.

(55) Lorenz, K.; Alves, E.; Roqan, I. S.; O'Donnell, K. P.; Nishikawa, A.; Fujiwara, Y.; Boćkowski, M. Lattice site location of optical centers in GaN:Eu light emitting diode material grown by organometallic vapor phase epitaxy. *Appl. Phys. Lett.* **2010**, *97*, 111911.

(56) de Boer, W. D. A. M.; McGonigle, C.; Gregorkiewicz, T.; Fujiwara, Y.; Tanabe, S.; Stallinga, P. Optical excitation and external photoluminescence quantum efficiency of  $\text{Eu}^{3+}$  in GaN. *Sci. Rep.* **2014**, *4*, 5235.

(57) Lorenz, K.; Vianden, R.; Birkhahn, R.; Steckl, A. J.; da Silva, M. F.; Soares, J. C.; Alves, E. RBS/Channeling study of Er doped GaN films grown by MBE on Si substrates. *Nucl. Instrum. Methods Phys. Res., Sect. B* **2000**, *161-163*, 946–951.

(58) Wahl, U.; Alves, E.; Lorenz, K.; Correia, J. G.; Monteiro, T.; de Vries, B.; Vantomme, A.; Vianden, R. Lattice location and optical activation of rare earth implanted GaN. *Mater. Sci. Eng., B* **2003**, *105*, 132–140.

(59) Filhol, J.-S.; Jones, R.; Shaw, M. J.; Briddon, P. R. Structure and electrical activity of rare-earth dopants in GaN. *Appl. Phys. Lett.* **2004**, *84*, 2841.

(60) Sanna, S.; Schmidt, W. G.; Frauenheim, Th.; Gerstmann, U. Rare-earth defect pairs in GaN: LDA+U calculations. *Phys. Rev. B: Condens. Matter Mater. Phys.* **2009**, *80*, 104120.

(61) Ofuchi, H.; Nishiwaki, T.; Takaba, K.; Ogawa, K.; Tabuchi, M.; Takeda, Y.; Wakahara, A.; Yoshida, A.; Ohshima, T.; Ito, H. Fluorescence EXAFS study on local structures around Eu atoms implanted in  $\text{Al}_x\text{Ga}_{1-x}\text{N}$ . *Phys. B* **2006**, *376-377*, 496–498.

(62) Ofuchi, H.; Honma, T.; Kawasaki, T.; Furukawa, N.; Nishikawa, A.; Fujiwara, Y. Fluorescence XAFS analysis of Eu-doped GaN layers grown by organometallic vapor phase epitaxy. *e-J. Surf. Sci. Nanotechnol.* **2011**, *9*, 51–53.

(63) Lupan, O.; Pauporté, T.; Viana, B.; Aschehoug, P.; Ahmadi, M.; Cuenya, B. R.; Rudzevich, Y.; Lin, Y.; Chow, L. Eu-doped ZnO nanowire arrays grown by electrodeposition. *Appl. Surf. Sci.* **2013**, *282*, 782–788.

(64) Geburt, S.; Lorke, M.; da Rosa, A. L.; Frauenheim, R.; Voss, T.; Kaiser, U.; Heimbrodt, W.; Ronning, C.; Ronning, C. Intense intrashell luminescence of Eu-doped single ZnO nanowires at room temperature by implantation created Eu-O<sub>1</sub> complexes. *Nano Lett.* **2014**, *14*, 4523–4528.

(65) Lorke, M.; Frauenheim, T.; da Rosa, A. L. Many-body electronic structure calculations of Eu-doped ZnO. *Phys. Rev. B: Condens. Matter Mater. Phys.* **2016**, *93*, 115132.

(66) Shannon, R. D. Revised effective ionic radii and systematic studies of interatomic distances in halides and chalcogenides. *Acta Crystallogr., Sect. A: Cryst. Phys., Diffr., Theor. Gen. Crystallogr.* **1976**, *32*, 751–767.

(67) Katchkanov, V.; Mosselmans, J. F. W.; O'Donnell, K. P.; Nogales, E.; Hernandez, S.; Martin, R. W.; Steckl, A.; Lee, D. S. Extended X-ray absorption fine structure studies of GaN epilayers doped with Er. *Opt. Mater.* **2006**, *28*, 785–789.

(68) Katsikini, M.; Kachkanov, V.; Boulet, P.; Edwards, P. R.; O'Donnell, K. P.; Brien, V. Extended X-ray absorption fine structure study of the Er bonding in  $\text{AlNO:Er}_x$  films with  $x \leq 3.6\%$ . *J. Appl. Phys.* **2018**, *124*, 085705.

(69) Wyckoff, R. W. G. *Crystal Structures*, 2nd ed.; Interscience Publishers: New York, 1963; Vol. 1, pp 85–237.